



HAL
open science

Role of point and line defects on the electronic structure of LaAlO₃ /SrTiO₃ interfaces

Alexandre Gloter, Giulio Tieri, Danfeng Li, Marco Caputo, Vladimir Strocov, Odile Stephan, J.-M M Triscone, Stefano Gariglio

► To cite this version:

Alexandre Gloter, Giulio Tieri, Danfeng Li, Marco Caputo, Vladimir Strocov, et al.. Role of point and line defects on the electronic structure of LaAlO₃ /SrTiO₃ interfaces. *APL Materials*, 2020, 8 (4), pp.041103. 10.1063/1.5132376 . hal-03004526

HAL Id: hal-03004526

<https://hal.science/hal-03004526>

Submitted on 13 Nov 2020

HAL is a multi-disciplinary open access archive for the deposit and dissemination of scientific research documents, whether they are published or not. The documents may come from teaching and research institutions in France or abroad, or from public or private research centers.

L'archive ouverte pluridisciplinaire **HAL**, est destinée au dépôt et à la diffusion de documents scientifiques de niveau recherche, publiés ou non, émanant des établissements d'enseignement et de recherche français ou étrangers, des laboratoires publics ou privés.

Role of point and line defects on the electronic structure of $\text{LaAlO}_3/\text{SrTiO}_3$ interfaces

Cite as: APL Mater. **8**, 041103 (2020); <https://doi.org/10.1063/1.5132376>

Submitted: 17 October 2019 . Accepted: 11 March 2020 . Published Online: 01 April 2020

Alexandre Gloter , Giulio Tieri, Danfeng Li , Marco Caputo, Vladimir N. Strocov , Odile Stéphan, Jean-Marc Triscone, and Stefano Gariglio 



View Online



Export Citation



CrossMark

ARTICLES YOU MAY BE INTERESTED IN

[Spin pumping and large field-like torque at room temperature in sputtered amorphous \$\text{WTe}_{2-x}\$ films](#)

APL Materials **8**, 041102 (2020); <https://doi.org/10.1063/1.5124688>

[New approaches for achieving more perfect transition metal oxide thin films](#)

APL Materials **8**, 040904 (2020); <https://doi.org/10.1063/5.0003268>

[Epitaxial stabilization of ultra thin films of high entropy perovskite](#)

Applied Physics Letters **116**, 071601 (2020); <https://doi.org/10.1063/1.5133710>

Hall Effect Measurement Handbook

A comprehensive resource for researchers

Explore theory, methods, sources of errors, and ways to minimize the effects of errors



Role of point and line defects on the electronic structure of LaAlO₃/SrTiO₃ interfaces

Cite as: APL Mater. 8, 041103 (2020); doi: 10.1063/1.5132376

Submitted: 17 October 2019 • Accepted: 11 March 2020 •

Published Online: 1 April 2020



Alexandre Gloter,^{1,a)} Giulio Tieri,^{1,2} Danfeng Li,^{2,b)} Marco Caputo,³ Vladimir N. Strocov,³ Odile Stéphan,¹ Jean-Marc Triscone,² and Stefano Gariglio^{2,c)}

AFFILIATIONS

¹Laboratoire de Physique des Solides, CNRS, Université Paris-Saclay, 91405 Orsay, France

²DQMP, Université de Genève, 24 Quai E.-Ansermet, 1211 Geneva, Switzerland

³Swiss Light Source, Paul Scherrer Institute, CH-5232 Villigen-PSI, Switzerland

^{a)}alexandre.gloter@u-psud.fr

^{b)}Present address: Department of Applied Physics, Stanford University, Stanford, CA 94305, USA.

^{c)}Author to whom correspondence should be addressed: Stefano.Gariglio@unige.ch

ABSTRACT

Realization of heterostructures containing multiple two-dimensional electron liquids requires a fine control of the fabrication process. Here, we report a structural and spectroscopy study of LaAlO₃/SrTiO₃/LaAlO₃ trilayers grown on the SrTiO₃ substrate by pulsed-laser deposition. Scanning transmission electron microscopy with the help of *ab initio* calculations reveals that antisite defects associated with oxygen vacancies are primarily present in the SrTiO₃ film (STO-f) close to the *p*-type interface (STO-f/LaAlO₃), while oxygen vacancies prevail close to the top *n*-type interface (LaAlO₃/STO-f). At the same interface, misfit dislocations relax the tensile strain of the top LaAlO₃ layer. Combining x-ray absorption spectroscopy, x-ray linear dichroism, resonant photoemission spectroscopy, and electron energy loss spectroscopy, we observe that the 3*d* orbital reconstruction at the interface between LaAlO₃ and the SrTiO₃ substrate is confined over a few interfacial Ti planes while, at the top *n*-type interface (LaAlO₃/STO-f), the absence of a dichroic signal can be related to the blurring of the interfacial orbital reconstruction due to the heterogeneity of defects.

© 2020 Author(s). All article content, except where otherwise noted, is licensed under a Creative Commons Attribution (CC BY) license (<http://creativecommons.org/licenses/by/4.0/>). <https://doi.org/10.1063/1.5132376>

INTRODUCTION

The observation of a two-dimensional electron liquid (2DEL) at the interface between two band insulators, namely, LaAlO₃ (LAO) and SrTiO₃ (STO),¹ has triggered widespread research activity with subsequent reports on various fascinating phenomena. Among them, superconductivity,² two-dimensional Shubnikov-de Haas conductance oscillations,³ and an efficient spin-to-charge conversion^{4,5} have been observed at the LaAlO₃/SrTiO₃ heterointerface. Recently, nano-devices⁶ and field-effect transistors⁷ have been realized based on this oxide interface, highlighting its potential for electronic applications.

The realization of heterostructures containing multiple two-dimensional electron liquids should open new possibilities, such as the engineering of the charge confinement in the STO layers, which could be useful, for instance, for the fabrication of quantum wells for

optical applications⁸ or the coupling of 2D superconducting gases. However, while the fabrication of several LAO/STO superlattices has been reported by several groups,^{9–12} a clear demonstration of the presence of several 2DELs is still lacking. A recent study aimed at realizing a multi 2DEL heterostructure has indeed highlighted the difficulty in obtaining conducting interfaces already on homoepitaxial STO films (STO-f).¹³ Two factors, linked to the STO layer, have been shown to control the interface conductivity: the stoichiometry and the chemical termination of the STO layer. A more recent work on epitaxially grown STO-f/LAO heterostructures on STO-substrates (STO-s) has similarly reported on the importance of eliminating ionic point defects to realize conductive interfaces.¹⁴ Several previous studies have pointed out the occurrence of point and linear defects, Sr/Ti non-stoichiometry and SrO type defects in STO homoepitaxial films,^{15–20} but these recent works clearly evidence the difficulties of maintaining the 2D electron liquid in such films.

Here, we investigate the crystalline and electronic structures of LAO/STO-f/LAO trilayers with various STO-f thicknesses [from 10 unit cells (uc) to 30 uc] by scanning transmission electron microscopy and x-ray spectroscopy. These structures give rise to the opportunity to study one *p*-type and two *n*-type interfaces:²¹ the first *n*-type interface, the traditional one, lies between the STO-s and the first LAO layer; the second *n*-type one forms when the second LAO layer is grown on top of the STO thin film, and, in between these *n*-type interfaces, the heterostructure naturally contains a *p*-type interface formed between STO-f and the first LAO layer. The structural properties of such a *p*-type interface have been less described,²¹ although recent reports on the occurrence of a two dimensional hole liquid highlight its interest.^{14,22}

The crystal structures are revealed by scanning transmission electron microscopy (STEM) with the support of *ab initio* calculations and the electronic structures are investigated by electron energy loss spectroscopy (EELS) at the atomic scale and by x-ray absorption spectroscopy (XAS), x-ray linear dichroism (XLD), and resonant photoemission (ResPE) on a macroscopic scale. This combination of techniques enables us to study the interplay between the cation, the charge, and the structural reconstruction (occurrence of point and line defects) in the LAO/STO interfacial system. The analysis of the first *n*-type interface (LAO/STO-s) reveals features common to traditional interfaces prepared on STO substrates: the LAO film is shown to be strained by the STO substrate and spectromicroscopy evidences a small amount of Ti³⁺ within a few nanometers close to the interface. STEM-EELS and XLD measurements confirm that a strong orbital hierarchy is observed at the first interfacial unit cells of the STO substrate.

The situation is very different for the interfaces with the STO film due to the occurrence of defects. Point defects (antisites) are present near the *p*-type STO-f/LAO interface in concert with a slight Sr/Ti off-stoichiometry. Point defects are also detected at the top of the STO-f near the interface with the second LAO film. The nature of the defects near the second *n*-type interface is uncertain but may imply a small number of vacancies, such as V_{Sr} or more probably V_O. Such defects are believed to trap the charge since a substantial amount of Ti³⁺ appears as in-gap states for this top interface. Furthermore, unit cell expansion of the STO-f due to the point defects and a concomitant network of misfit dislocations are observed at this interface. The dislocations partially relax the epitaxial strain on the LAO film. At this top interface, the orbitals hierarchy observed by XLD measurements is suppressed, which might be related to the observed defects and structural heterogeneity or to the different charge confinement due to the defects and/or to the STO layer thickness.

This work clearly evidences that a small amount of defects can strongly alter the whole electronic structure of the LAO/STO interface. In particular, hierarchy of the d_{xy} vs (d_{yz} , d_{xz}) orbitals is shown to be highly sensitive to the local reconstruction of the interface, offering further possibility to engineer it.

EXPERIMENTAL

Sample growth

LAO/STO-f/LAO heterostructures were grown by pulsed-laser deposition (PLD) from single-crystalline targets on (001)-oriented

TiO₂-terminated STO substrates in conditions similar to those reported in Ref. 13. The laser fluence was set to ≈ 0.6 J cm⁻², and the repetition rate was kept at 1 Hz. The growth was monitored by reflection high-energy electron diffraction (RHEED), recording the evolution of the intensity of the specular spot to estimate the layer thickness. The STO films were grown at 800 °C in an oxygen pressure of 8×10^{-5} Torr and at 1100 °C in an oxygen pressure of 1×10^{-6} Torr. The LAO layers were grown at 800 °C in an oxygen pressure of 8×10^{-5} Torr. The samples characterized in this work are classified into two categories depending on the fabrication process. For convenience and consistency with our previous work,¹³ we name them *in situ* samples and *ex situ* samples. For *in situ* samples, the STO thin film is grown at 1100 °C just after the LAO layer, without breaking the vacuum. Three *in situ* samples have been investigated: LAO(10 uc)/STO-f(15 uc)/LAO(10 uc), LAO(10 uc)/STO-f(30 uc)/LAO(10 uc), and LAO(10 uc)/STO-f(30 uc)/LAO(5 uc). For the *ex situ* samples, an additional *ex situ* surface treatment (buffered-HF etching followed by a high-temperature annealing procedure) of the STO layer (deposited at 800 °C) has been done before the deposition of the second LAO film. Two *ex situ* samples have been investigated: LAO(10 uc)/STO-f(10 uc)/LAO(10 uc) and LAO(10 uc)/STO-f(20 uc)/LAO(10 uc). In addition a conventional LAO(10 uc)/STO-s sample has been grown and used as a control interface, notably for synchrotron measurements (where only the top interface is probed). The thickness of the LAO layer (10 uc) is chosen, on one side, in order to avoid the chemical intermixing at the interfaces with STO to dominate the observations²¹ as would happen for thinner layers and, on the other side, in order to prevent the relaxation of the epitaxial strain occurring above 25 uc²³ as well as the degradation of the interface conductivity appearing above 10 uc.²⁴

STEM-EELS

Scanning transmission electron microscopy has been performed using a Cs corrected Nion USTEM microscope. The operating voltage is 100 keV in order to limit the beam damage. The electron energy loss spectra were acquired using a modified Gatan spectrometer. The EELS aberrations are corrected up to the third order, resulting in an overall energy resolution of 300–400 meV at the core-loss. The overall stability of the system allows an energy shift of ~ 10 meV to be measured over several minutes. A back-illuminated electron-multiplying CCD (EMCCD) camera is used as a final EELS detector, allowing a high electron sensitivity. The amount of Ti³⁺ near the interfaces has been quantified by fitting the EELS data with reference spectra. For Ti⁴⁺, this comes from the SrTiO₃ substrate. For Ti³⁺, experimental LaTiO₃, DyTiO₃, or a computed Ti³⁺ spectra in Oh symmetry²⁵ have been used. The fitting deviation for the different Ti³⁺ references is well below 5%. The main source of uncertainty results from the intensity normalization procedure of the Ti³⁺ and Ti⁴⁺ reference spectra. They have been normalized beyond the white lines, i.e., ~ 10 to -15 eV above the edge onset, in order to avoid solid state effects, such as a change in the *3d* occupations among the references. Such a normalization procedure could be biased by thickness variation, edge subtraction issues, resulting in an estimated inaccuracy of $\sim 10\%$. Others factors, such as the signal to noise ratio of the atomically resolved Ti-L edge, will also limit the accuracy. The overall inaccuracy of the Ti³⁺ quantification by EELS is estimated below 20%.

Samples were mostly prepared by conventional mechanical polishing (MultiPrep System from Allied High Tech) combined with a gentle ion milling (Gatan PIPS2, final milling performed at low voltages <1 keV). Some samples were prepared by using the focused ion beam and showed similar results.

XAS-XLD and ResPE

Synchrotron measurements were done at the soft-X-ray ARPES endstation²⁶ of the ADDRESS beamline at the Swiss Light Source, Paul Scherrer Institute. The x-ray linear dichroism (XLD) of the Ti *L* edges was measured in total electron yield mode by switching the horizontal and vertical polarizations. The x-ray grazing incidence angle was 20°, and the samples were maintained at room temperature. ResPE spectra were collected for energies spanning from 455 eV to 470 eV while the samples were cooled to a temperature of ~15 K.

Ab initio calculations

Ab initio calculations have been performed using density functional theory as implemented in the Castep package.²⁷ A local exchange-correlation functional has been used.²⁸ Ultrasoft pseudopotentials with 6, 12, and 10 valence electrons have been used for O, Ti, and Sr atoms, allowing a small plane-wave energy cutoff of 380 eV. The $3 \times 3 \times 3$ (135 atoms) and $3 \times 3 \times 4$ (180 atoms) supercells have been used for the defective models with one and two antisites, respectively. A Monkhorst–Pack *k*-point sampling based on a $2 \times 2 \times 2$ grid has been used. Geometric optimization has been performed until variations in forces and energies were below 0.03 eV/Å and 10^{-5} eV/atom.

RESULTS

Point and line defects

Figures 1(a) and 1(b) reveal the atomic structure of the *in situ* LAO(10 uc)/STO-f(30 uc)/LAO(10 uc) heterostructure observed in

STEM high-angle annular dark field (STEM-HAADF) and STEM bright-field (STEM-BF) imaging along the [100] direction. The two LAO layers are clearly visible as brighter stripes in the HAADF image due to the sensitivity of this technique to the large atomic number of La atoms ($Z = 57$). The contrast of the image acquired in STEM-BF, a technique very sensitive to structural aspects such as crystallographic disorder, has been enhanced to better reveal faint modifications in the STO structure. The STO substrate appears very homogeneous, indicating a perfect crystallinity, while the STO thin film has faint blurred contrast nearby both interfaces. At the *p*-type interface (the one with the first LAO layer), some white contrasted lines extending over several nanometers can be seen either parallel or perpendicular to the interface plane. Beside these lines, small dark faint contrasts are visible and extend over several nanometers (up to 10 nm at some places) from the interface. The STO-f near the top (*n*-type) interface with the second LAO layer displays a different BF contrast. There are no visible white lines, but a faint dark contrast can be seen and extends typically up to 2–3 nm in the STO film. The main striking defects occurring at this LAO/STO-f interface are misfit dislocations, clearly visible in the STEM-HAADF image [Fig. 1(c)]. Details of the dislocation cores and the additional LAO planes are shown in Figs. 1(d) and 1(e). We notice that dislocations were also present for samples grown at 800 °C and for smaller STO-f thicknesses (see Fig. SI-1 in the supplementary material).

Investigation of the white lines that propagate from the STO-f/LAO interface into the STO film reveals that the contrast observed in the BF image originates from the Ti columns. A zoom of this disorder region, shown in Fig. 2(a), evidences one atomic column with a doublet/dumbbell feature while the two neighboring columns show an elongated distorted contrast. While the interpretation of the STEM-BF contrast is not straightforward, we suggest that the doublet columns correspond to atoms located 80 pm off the Ti-site position.

Figures 2(b) and 2(c) show STEM-HAADF and STEM-annular bright field (ABF) images of an heavily defective STO-f area close to the *p*-type interface. Such a highly defective part can be observed

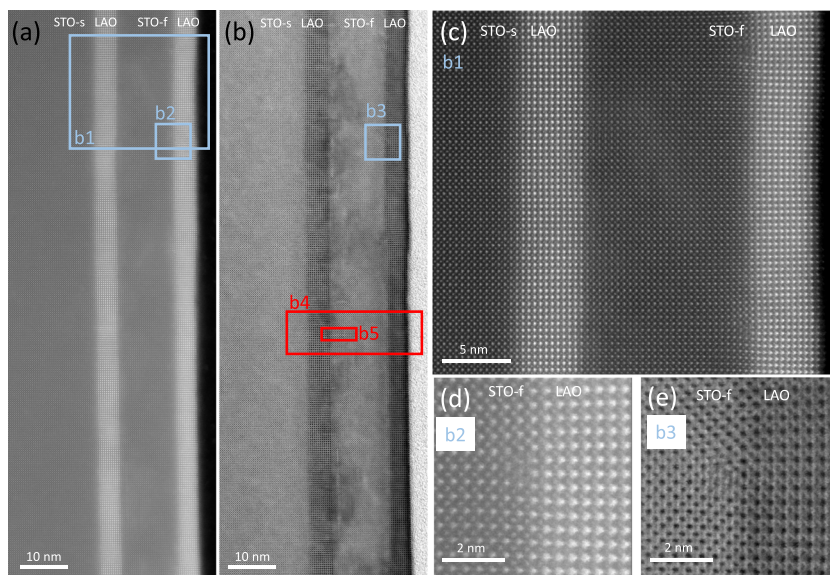


FIG. 1. (a) STEM-HAADF and (b) STEM-BF of the LAO(10 uc)/STO-f(30 uc)/LAO(10 uc) multilayer. BF contrast has been saturated to evidence faint features. Squared boxes indicate the areas for the zoomed images. The boxes b4 and b5 are enlarged in Fig. 2. (c) STEM-HAADF showing the presence of misfit dislocations at the top LAO/STO-f interface. (d) STEM-HAADF and (e) STEM-BF images of a dislocation.

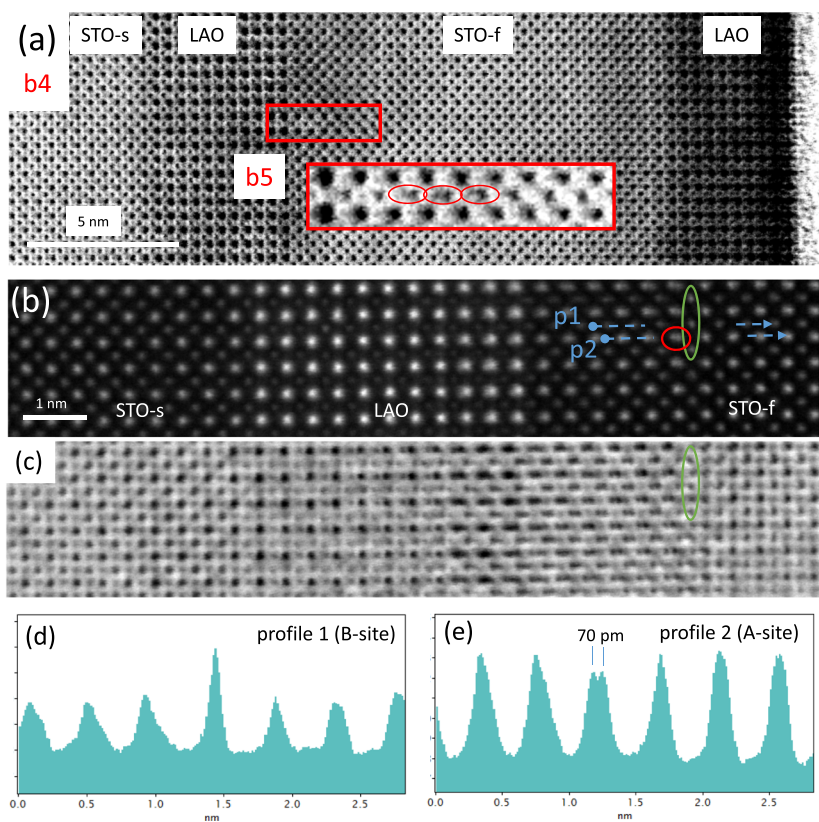


FIG. 2. (a) STEM-BF with saturated contrast. The STO-s is “perfect,” but the STO-f has defects at both interfaces. At LAO/STO-f, some of the defects show line geometries. (b) STEM-HAADF and (c) STEM-ABF of highly defective STO-f close to first LAO layers. The green oval shows B sites with much higher HAADF contrast. (d) Profile 1 of the HAADF showing the high intensity due to the Sr atom in the Ti site. (e) Profile 2 of the HAADF along A sites next to the antisite. Typically, a maximum off-centering of 70 pm is observed in this defective area.

occasionally and, although not being representative of the average amount of defects near the interface, might help decipher the nature of these defects. The STEM-HAADF image evidences a relatively well ordered STO structure. However, 3 B-site atomic columns, circled in green, exhibit a much higher contrast [see the intensity profile plotted in Fig. 2(d)]. This indicates that several Ti atoms have been replaced, most probably, by Sr atoms in these columns. The first-neighboring A-sites of these Sr-antisites show a doublet whose separation is ~ 70 pm, as seen in the profile of Fig. 2(e), indicating substantial distortion and off-centering. The presence of several doublets is also revealed in the STEM-ABF image [Fig. 2(c)], which, being very sensitive to the structure and also to light elements, seems to indicate that a distorted STO structure is overlapping with a more ordered structure. The maximum displacement is also measured at about 80 pm in the ABF image near the position of Sr-substituted B sites. The ABF image resolves much more additional columns than the HAADF one in the defective area, and thus, the defects also involve a strong rearrangement of the oxygen network beside the cation antisites.

Many types of point defects (vacancies, adatoms, and antisites) or clusters of point defects have been suggested for bulk STO and STO thin films^{17,29–32} but also more specifically for the LAO/STO interface such as Ti-on-Al antisites, which are believed to reduce the polar discontinuity.³³ For STO, antisites, where Sr replaces Ti (Sr_{Ti}) or vice versa, have been reported and resulted in a substantial off-centering of the antisite atoms.^{30–32} According to *ab initio*

calculations, such antisite Sr_{Ti} defects, together with oxygen vacancies (V_{O}), are the most stable defects in a Sr-rich environment.³⁴ They result in a 81 pm off-centering along the [100] direction³² and have been experimentally observed to generate nanopolar regions.³¹ When the cation non-stoichiometry is larger (e.g., $\text{Sr}/\text{Ti} > 1.1$), several transmission electron microscopy studies evidence the formation of Ruddlesden–Popper (RP) planar faults.^{15–17,29,35} Thus, it appears that, in our case, the local Sr/Ti imbalance is too weak to produce RP-type defects but might give rise to a local clustering of point defects, such as strontium antisites and oxygen vacancies. *Ab initio* calculations reported in Figs. SI-2–4 reveal that such clustering is energetically favorable. Binding energies of ~ -1.64 eV are obtained for defects composed of $(\text{Sr}_{\text{Ti}}-\text{V}_{\text{O}})$ complexes. A $(\text{Sr}_{\text{Ti}}-\text{V}_{\text{O}})_2$ dimer results in a small defective planar structure with atoms off-centered by typically 60 pm (see Figs. SI-3 and 4), compatible with the microscopic observation.

Inhomogeneous contrast modulations of the STO-f at the top interface are even fainter and do not evidence geometric features such as lines or obvious atomic off-centering. One possibility here is that point defects are in lower concentration and do not cluster. STEM-HAADF imaging does not reveal the presence of strontium vacancies (V_{Sr}), previously observed in homoepitaxial STO,¹⁸ or other cationic defects, despite its high sensitivity to such vacancies. The occurrence of oxygen vacancies, whose imaging is most difficult at low concentration, has also been suggested for LAO/STO^{14,36} and might primarily compose the point defects at this interface.

Actually, the exact nature of the point defects near the top of the STO-f is impossible to determine solely on the microscopic images. The main observable defects at this top interface are extended line defects, i.e., misfit dislocations. Cubic STO has a bulk lattice parameter $a_{\text{STO}} = 0.3905$ nm and the pseudo cubic unit cell of rhombohedral LAO has a parameter $a_{\text{LAO}} = 0.3792$ nm so that the LAO layer is under a tensile strain $(a_{\text{LAO}} - a_{\text{STO}})/a_{\text{LAO}} = -3\%$. Misfit dislocations partially relax such elastic strain in the top LAO layer. Geometric Phase Analysis (GPA)³⁷ has been conducted to evaluate the strain distribution within the whole series of layers. Figure 3(a) shows the map of the ratio between the out-of-plane (c) and the in-plane (a) lattice parameters for a LAO/STO-f(30uc)/LAO/STO-s heterostructure. The profile of the c/a ratio, plotted in Fig. 3(b) for a region in-between two dislocations, evolves from a value of 1 in the STO substrate—chosen as reference in the GPA procedure—to a first maximum of 1.01 before the interface with LAO. Such an increase signals a c -axis expansion, already observed by several groups,^{38–43} while the in-plane parameter remains constant across this bottom interface.

Our GPA results, as well as direct measurements of the atomic displacements, indicate that the maximum of the c expansion occurs 2 unit cells before the interfacial plane, in line with previous reports (see Ref. 39). This means that the Ti atoms located at the interface (in the case of a perfect SrO–TiO₂–LaO sequence as expected for a model n -type interface) actually have a c/a ratio close to or already slightly below 1. Previously published works, notably using STEM-ABF imaging, reveal that small polar distortions are present in the STO in the vicinity of the interface^{39,43} and contribute to the c expansion. Our STEM-HAADF imaging also confirms a small Ti off-centering present in STO-s next to the interface, which might be related to a small polar distortion (see Fig. SI-5). Concerning the first LAO layer, the c/a ratio decreases to ≈ 0.96 . This value is in perfect agreement with a purely elastic deformation imposed by the STO

substrate and a Poisson ratio for LAO of 0.24, which together reduce the c_{LAO} lattice parameter to 0.374 nm.²³

Although appropriate STEM-ABF imaging (for instance, along the [110] zone axis) was not done to determine the balance between the anti-ferro-distortive rotation and the polar distortion in the first LAO film, we observe by HAADF an extremely small Al off-centering (see Fig. SI-5), with an intensity comparable to that reported for thicker LAO layers where the internal electric field is reduced.⁴³

The situation at the top LAO/STO-f interface is very different. While the c/a ratio is close to unity in the central part of the STO-f, it expands approaching the top interface. The expansion extends over the whole defective area and notably up to the last interfacial plane. The second LAO film shows a c/a ratio that now fluctuates close to 1, demonstrating that the dislocation network has substantially relaxed the LAO top layer. The role of the dislocations on the strain distribution appears obvious when looking at the c/a profile plotted in Fig. 3(c). In front of a dislocation core, the STO-f encounters a strong tensile local strain ($c/a < 1$), while the LAO layer beyond the dislocation core shows a strong local compressive strain ($c/a > 1$). STEM-HAADF imaging also confirms that off-center positioning of the B cation can occur near the LAO/STO-f interface. Nevertheless, strong structural heterogeneities of the STO film are present at this second interface and a polar-type distortion is more difficult to quantify by HAADF imaging, notably near the dislocations. Only strain maps were thus quantitatively achieved at this interface. The strain distribution for trilayers with thinner STO-f and prepared by an *ex situ* growth approach can be seen in Fig. SI-6. The STO-f is only 10 uc thick and is almost expanded everywhere as compared to the STO substrate. This is in agreement with an expansion extending over several nanometers due to the STO-f point defects. We note that the presence of misfit dislocations does not depend on the thickness of the STO layer, since we also observed partial relaxation of the LAO

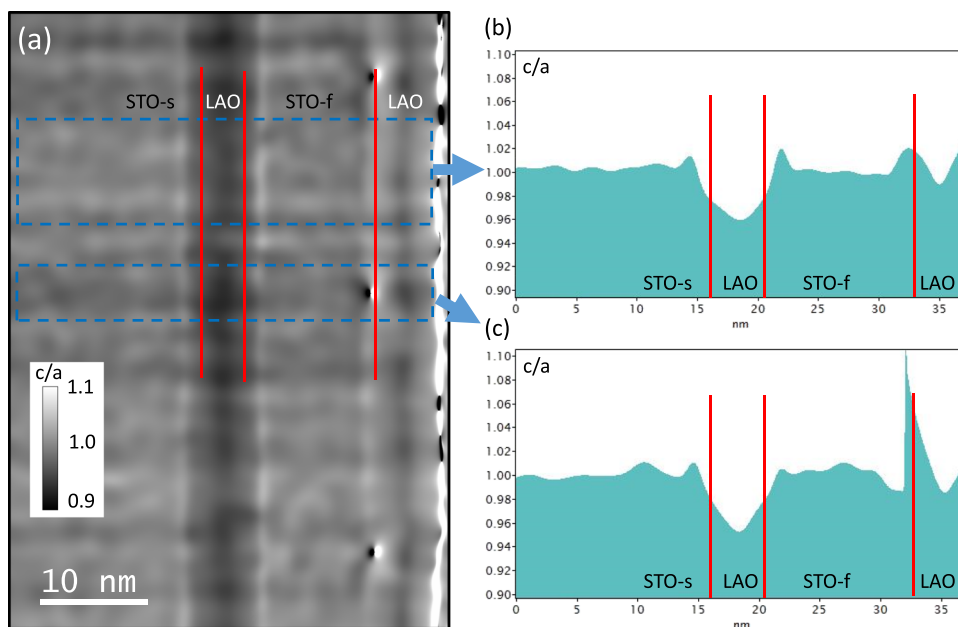


FIG. 3. (a) c/a map obtained from GPA analysis of the HAADF images from the LAO/STO-f(30 uc)/LAO multilayer. (b) and (c) c/a profiles extracted from a region in-between the dislocations and across a dislocation core. The red lines indicate the interfacial atomic plane as determined from the HAADF image.

layers grown on top of a 10 uc. STO-f. To summarize the main structural aspects of the two *n*-type interfaces, the bottom LAO/STO-s interface is in agreement with the previously reported studies. On the other hand, the top LAO/STO-f interface has a very different structural character. Defective areas with point defects and cell volume expansions are observed in the top part of the STO-f, with the strain in the LAO layer partially relaxed by the presence of misfit dislocations. Such structural difference might change the balance between polar and anti-ferro-distortive distortions at this interface but could not be described solely based on HAADF imaging. Concerning the *p*-type interface, Sr_{Ti} antisite defects appear to be the main point defects in the STO-f, displacing off-center the neighboring Sr columns. Small polar distortion is also observed in the STO-f near that interface.

Stoichiometry at *n*- and *p*-type interfaces

STEM-EELS has been used to determine the chemical profile of these heterostructures: it enables us to reveal the atomic planes at

the interfaces (TiO₂/LaO vs SrO/AlO₂) and to estimate the interdiffusion level of the cations between the layers. Typical EELS spectra of LAO and STO areas can be seen in Fig. 4(a): the energy range encompasses the Ti-L (450 eV), O-K (530 eV), La-M (830 eV), Al-K (1560 eV), and the Sr-L (1940 eV) edges, allowing for a simultaneous quantification of all the cations. The resulting chemical profile of the three interfaces of the LAO/STO-f (30 uc)/LAO/STO-s heterostructure is displayed in Fig. 4(b). The interface with the more abrupt plane termination is the top LAO/STO-f one. For this interface, the four curves corresponding to Sr and Ti on one side and La and Al on the other side are well separated and the corresponding planes sequence is clearly SrO–TiO₂–LaO–AlO₂, confirming an *n*-type interface. The bottom LAO/STO-s interface is also primary *n*-type (TiO₂-terminated STO), despite some cationic intermixing. The middle STO-f/LAO interface is different and exhibits a SrO rich first plane at the STO side that indicates *p*-type. We note that similar plane terminations are observed for the samples grown at 800 °C, i.e., slightly intermixed *n*- and *p*-type interfaces for the first LAO layer and a sharper *n*-type one at the LAO/STO-f interface. It

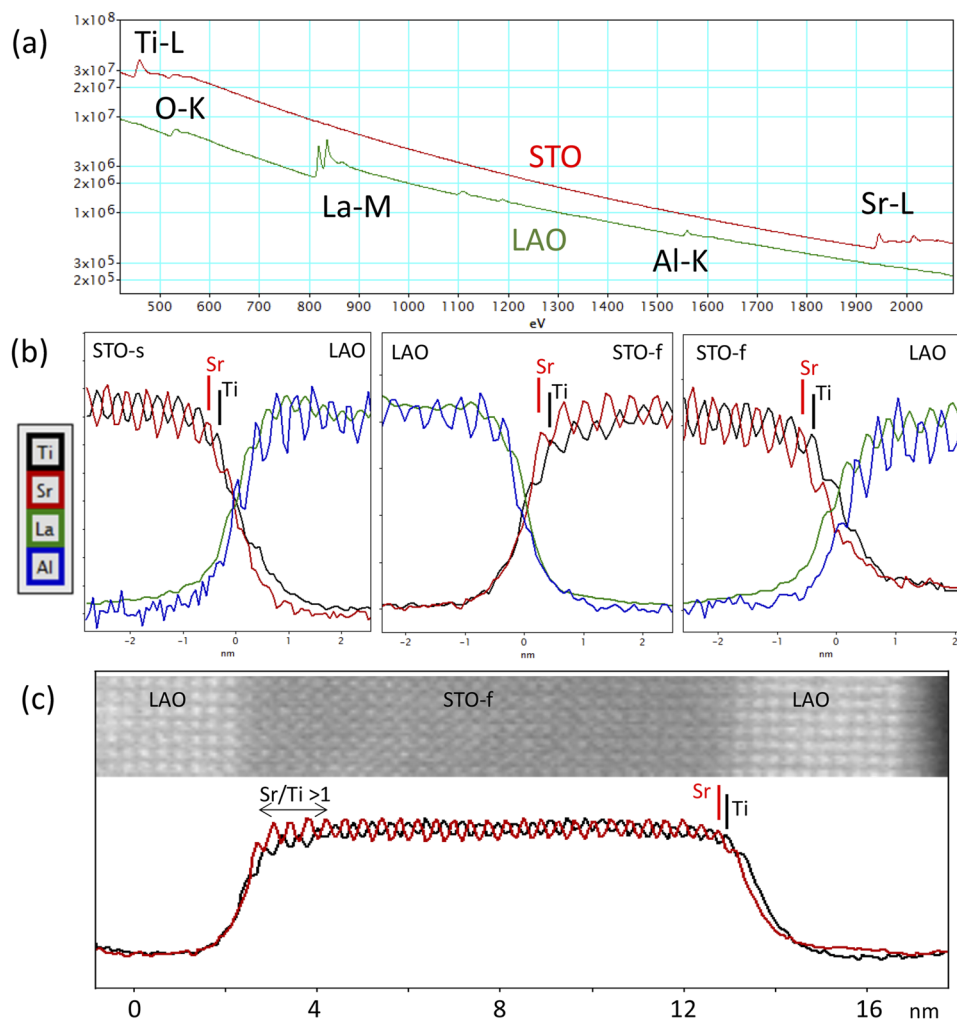


FIG. 4. (a) EELS spectra of LAO and STO measured at small dispersion in order to collect Ti-L, O-K, La-M, Al-K, and Sr-L. (b) EELS intensities of the various edges showing the plane termination from STO-s/LAO/STO-f(30uc)/LAO multilayers. (c) EELS Sr/Ti profile showing an off-stoichiometry of the STO-f close to the first LAO layer. From left to right: *p*-type STO-f/LAO and *n*-type LAO/STO-f interfaces.

demonstrates that both fabrication approaches are valid to obtain a TiO_2 -terminated surface of a STO layer, as reported previously.¹³

Figures 4(c) and SI-7 show the Sr and Ti profiles over the whole LAO/STO-f/LAO/STO-s heterostructure for a 1100 °C sample and an 800 °C one, respectively. A small but clear Sr enrichment ($\text{Sr}/\text{Ti} > 1$) is present over the first 4–5 unit cells of the STO-f. Since La and Al do not diffuse so far in the STO-f (and have symmetric decays), this EELS measurement indicates a small Sr excess in the first unit cells of the STO-f. This observation, in line with the detection of the Sr antisites in the HAADF images, indicates a small non-stoichiometry of the *p*-type interface. For the rest of the layer up to the LAO/STO-f interface, the Sr/Ti ratio remains closer to 1. The nature of the point defects in the STO-f near the second LAO layer is not made clearer by the EELS cationic study, which strengthens the possible role of oxygen vacancies or that of very diluted cationic vacancies.

Vertical extension of Ti^{3+}

STEM-EELS measurements have also been performed with higher energy resolution in order to quantify the amount of Ti^{3+} in the STO-s and STO-f at both bottom (LAO/STO-s) and top

(LAO/STO-f) interfaces. Quantification of Ti^{3+} by EELS is based on the analysis of the Ti- $L_{2,3}$ edge that corresponds to a quasi-atomic transition from a $3d^n$ ground state to a $c3d^{n+1}$ excited state (where *c* is a hole in the Ti $2p$ orbital).

Figure 5(a) displays an intensity map of the Ti- $L_{2,3}$ edge acquired to quantify the amount of Ti^{3+} : the map and the projection along the interface direction (panel b) reveal the atomic resolution achieved by the technique. Fitting the EELS spectra shown in Figs. 5(d) and 5(e) with reference data for Ti^{3+} and Ti^{4+} , one can quantify the amount of Ti^{3+} .

The occurrence of Ti^{3+} can also be seen directly, since it appears as an additional intensity in-between the $L_3 - e_g$ and $L_3 - t_{2g}$ peaks. Due to sufficient signal to noise ratio, even a small amount of Ti^{3+} can be quantified: the spectra in panels (d) and (e) correspond to 0.03 and 0.1 Ti^{3+} per Ti atom, respectively. The Ti^{3+} fraction estimated across the two interfaces is plotted in Fig. 5(c). At the STO-s side, the amount of Ti^{3+} near the interface is small (below 0.05 per unit cell), but extends over a dozen of nanometers. Integrating over the whole Ti^{3+} distribution yields a total charge of 0.55 ± 0.11 electrons/surface uc. In the case of the STO film, Ti^{3+} is only strongly present in a narrower region near the top *n*-type interface. This is

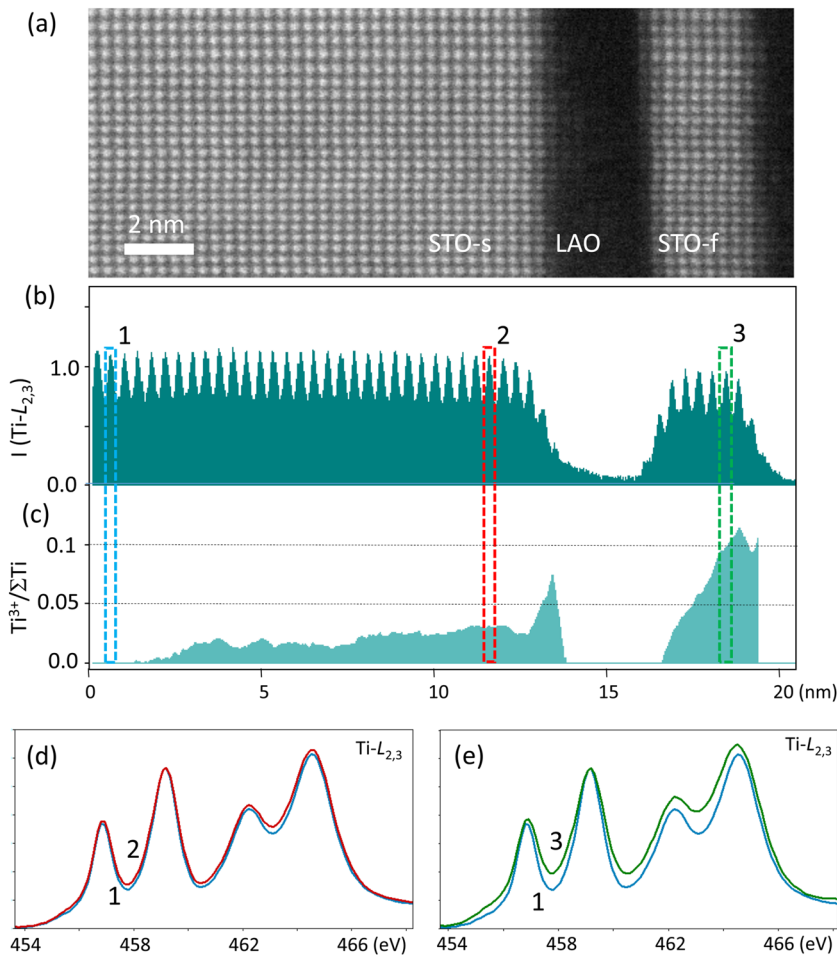


FIG. 5. (a) Map obtained from the EELS Ti-L intensity of the spectrum image from a STO-s/LAO/STO-f(10uc)/LAO. (b) Ti-L EELS intensity profile and (c) corresponding Ti^{3+} contribution. (d) EELS spectra for the STO-substrate (position 1, blue line) and 0.03 Ti^{3+} (position 2, red line). (e) EELS spectra for the STO-substrate (position 1, blue line) and 0.10 Ti^{3+} (position 3, green line).

observed for the thinnest 10 uc STO-f (Fig. 5) but also for the thicker 30 uc STO-f (see Fig. SI-8). Despite Ti^{3+} being only present over few nanometers, its large quantity per unit cell (≈ 0.1 electrons/uc) results in a total integrated amount of 0.45 ± 0.09 electrons/surface uc. The Ti^{3+} estimates for the two n -type interfaces are compatible with the theoretical predictions based on the polar discontinuity and comparable with previous spectroscopic works based on core-level photoemission,^{44,45} EELS,^{21,40} and RIXS.⁴⁶ We note that the charge estimated from the integrated EELS Ti^{3+} signal is significantly higher than the one extracted from electric transport, indicating that part of the carriers at these interfaces is localized. The overall distribution of the Ti^{3+} in the heterostructure corresponds to a $n/p/n$ -type

interface sequence. XAS measurements collected in TEY mode and shown in Fig. 6(a) confirm the difference in the Ti^{3+} amount, which is located just next to the two interfaces. The first n -type interface exhibits a Ti-L edge very similar to previous reports on conductive LAO/STO,^{47–49} where the Ti^{3+} contribution is barely observable, while the spectra of the top n -type interface have a clear Ti^{3+} component.

Figures 6(b) and 6(c) show resonant PES measurements for both interfaces. While in the LAO/STO-s interface, one does not observe in-gap states (IGS), a clear peak is observed at ~ 1.8 eV below the Fermi level for the LAO/STO-f. The origin of the IGS in STO has been debated. The polaronic effect,⁵⁰ spectral weight transfer

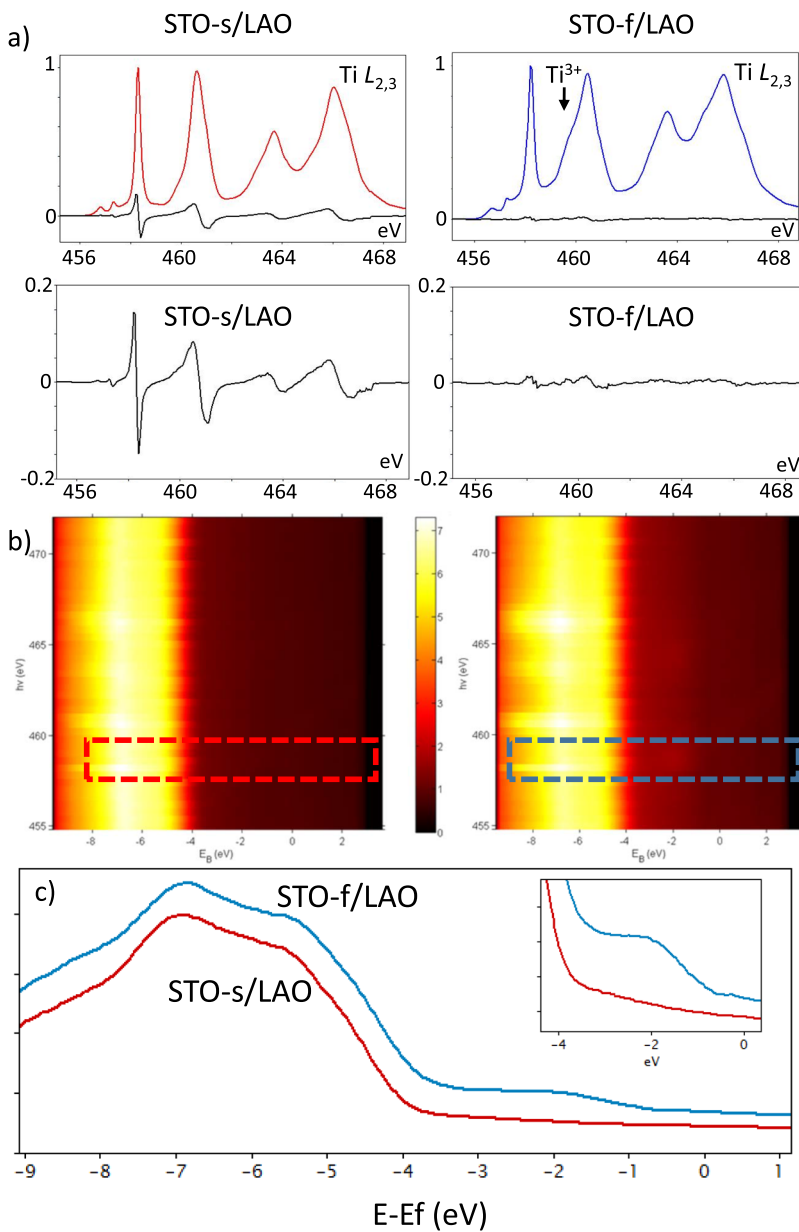


FIG. 6. (a) XAS $\text{Ti} L_{2,3}$ isotropic spectra for LAO/STO-s and for LAO/STO-f(10uc)/LAO/STO-s samples. The presence of a stronger Ti^{3+} contribution can be seen at the LAO/STO-f interfaces. A linear dichroism (XLD = in-plane-out-of-plane) is measured for the (LAO/STO-s) interface, while it is negligible at the top one (LAO/STO-f) interface. The XAS and XLD spectra have been normalized to the $\text{Ti} L_3$ maxima. (b) ResPE for the two interfaces. (c) ResPE profiles of the resonant photo-emission extracted at ~ 459 to 460 eV showing in-gap states at the LAO/STO-f interface.

from the coherent states for doped STO,⁵¹ and impurity levels have been reported.^{52,53} In the context of the LAO/STO-s interface, recent angle resolved photo-emission spectroscopy combined with *ab initio* dynamical mean field theory calculations concluded that such in-gap states correspond to Ti^{3+} with $e_g(x^2 - y^2)$ character related to the presence of oxygen vacancies.⁵² Since point defects are observed near the LAO/STO-f interface, the IGS might also be derived from defect levels. The binding energies for the IGS associated with oxygen vacancies at the LAO/STO-s are reported in the 1.2–1.5 eV energy ranges.^{52,54} The 1.8 eV binding energy is thus larger. Nevertheless, IGS has been reported at a binding energy of up to 2.2 eV in the case of oxygen vacancies located exactly at the interface between STO and Al_2O_3 spinel.⁵⁵ Since the LAO/STO-f interface has a different structure with respect to the traditional LAO/STO-s interface and notably a larger cell expansion at the interface, the number of oxygen vacancies and the quantum well at this interface could be different and might explain the binding energy shift with respect to a traditional interface. Another possibility is that the point defect contributing to the IGS in the STO-f/LAO interface might not be the primary oxygen vacancy and was too diluted to be observed by STEM-EELS.

Ti 3d orbital ordering

A Ti 3d orbital ordering has been reported at the LAO/STO interface. While each t_{2g} and e_g 3d orbital manifold is quasi-degenerate in bulk cubic STO, a hierarchy has been demonstrated to take place at the interface with LAO. XAS-XLD^{47–49} and ARPES^{56,57}

measurements, supported by *ab initio* modeling,^{58–62} indicate that at the interface, close to the Γ point, d_{xy} orbitals lie lower in energy than d_{xz}/d_{yz} states. For our heterostructures, the comparison of the linear dichroism of a standard LAO/STO-s sample with the one of the LAO/STO-f interface reveals that only the former exhibits an orbital order, while for the interface between the two layers, the dichroic signal is absent, as shown in Fig. 6(a).

In a STEM-EELS experiment, linear dichroism is difficult to achieve, notably with atomic resolution. Nevertheless, the orbital hierarchy might leave a small fingerprint also in the isotropic spectra. According to the work of Salluzzo *et al.*,⁴⁷ the intensity of the XLD signal is correlated with a shift toward higher energy of the $L_3 e_g - b_1$ peaks. For a LAO/STO interface with more than 4 uc of LAO where the XLD signal is fully expressed, the energy shift is 50 meV. Our calculation of the Ti L spectra using multiplet techniques²⁵ (see Fig. SI-9) confirms that t_{2g} and e_g splittings could be accompanied with an upward shift of the isotropic spectra, notably in the $L_3 e_g - b_1$. Assuming a 200 meV splitting of the t_{2g} manifold at the Γ point^{60,61} (see Sec. VII of the [supplementary material](#)), we obtain an energy shift up to 50 meV. Nevertheless, it has to be noted that such calculations are qualitative and not exclusive as several other modifications to parameters might result in rather similar energy shifts.

Figure 7 displays the EELS Ti L edges measured at different positions from an area comprising a dislocation at the top interface. The layers are visible in the atomically resolved HAADF image of Fig. 7(a). A map of the c/a ratio has been overlapped and shows the same features as previously described: in particular, the second interface has an inhomogeneous c/a ratio and a strong

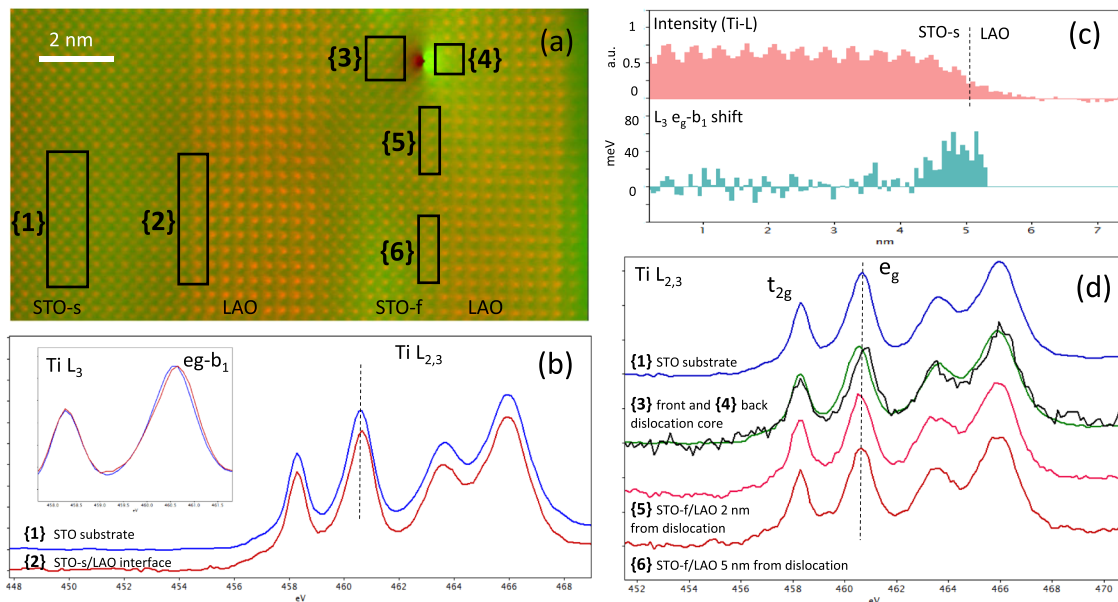


FIG. 7. (a) STEM-HAADF overlapped with a c/a image obtained from a GPA analysis. The layers and position of the dislocation are easily seen. Numbered squares indicate the approximate position of the extracted spectra (on-line DF is a bit more distorted) (b) EELS $Ti-L_{2,3}$ from the STO substrate {1} and the interfacial signal with LAO {2}. In the onset, a small shift of the $L_3 e_g - b_1$ line can be seen. (c) Profile of the intensity of the Ti-L edge enables us to determine the position of the interfacial TiO_2 plane. It can be compared with the $Ti-L_3 e_g - b_1$ energy shift. (d) Various EELS $Ti-L_{2,3}$ edges extracted next to the dislocation cores {3} and {4} or at the interface between the STO film and LAO {5} and {6}. A spectrum from the STO substrate {1} is shown for comparison. Dashed lines are guides for the eye.

tensile/compressive doublet around the core dislocation. Figure 7(b) compares the EELS Ti $L_{2,3}$ spectra acquired at the STO substrate and at the very last TiO_2 plane of the LAO/STO-s interface. The differences between the spectra consist in some additional intensity in-between the L_3 lines (due to the Ti^{3+} contribution) and a small shift of the $L_3 - e_g$ line. The energy shift of the $L_3 - e_g$ line, albeit small, can be robustly measured and appears homogeneous along the interface, while not such a clear shift was obtained on the L_2 line. When measured across the interface, looking at the plot in Fig. 7(c) together with the intensity of the Ti L spectra, one observes a shift of roughly 40 meV for the last TiO_2 plane, which vanishes rapidly (for EELS detection) for the third TiO_2 plane away from the interface. The value of the energy shift at the interfacial TiO_2 plane is in qualitative agreement with a strong orbital hierarchy occurring right at the interface, where the environment is highly non-symmetrical (SrO– TiO_2 –LaO). Actually, the L_3 peak shift measured by EELS is only an indirect probe of the interfacial orbital anisotropy of the Ti-3d state in this system. Such isotropic EELS measurements would not be sensitive to orbital ordering in a different context, e.g., to a weaker orbital hierarchy propagating farther from the interface.

Nevertheless, it confirms several *ab initio* calculations that have indicated a strong d_{xy} vs d_{yz}/d_{xz} splitting only for the interfacial states. Zhong *et al.*⁶¹ calculated an energy splitting of ~ 250 meV between d_{xy} and d_{yz} orbitals at the Γ -point for the interfacial Ti electrons, which vanishes already at the third titanium layer where the electron population of the different t_{2g} orbitals becomes equal. Deeper into the substrate, first-principles calculations by Delugas *et al.*⁶⁰ and Popović *et al.*⁶³ demonstrated a population inversion, with the d_{xz}/d_{yz} orbitals becoming the states with the lowest energy.

For the top n -type interface, i.e., at the LAO/STO-f interface, the EELS Ti-L fine structures are very heterogeneous [see Fig. 7(d)]. First, while comparing Ti-L edges from STO-f areas located in front and at the back of the dislocation core where substantial tensile strain and compressive strain are present, respectively, clear negative and positive energy shifts of the e_g line are observed. While the splitting between t_{2g} and e_g measured by EELS is of 2.29 eV at the STO substrate, it increases to 2.55 eV in the compressive part of the dislocation. Such an increase of ~ 250 meV of the crystal field splitting is massive but is not surprising at the dislocation core where consequent compression and distortion ($c/a > 1.1$) are present. For instance, changes in crystal field splitting of ~ 250 meV are typical for transition metal monoxides under high compression of ~ 100 GPa.⁶⁴ A substantial part of the observed changes in the Ti crystal field splitting might thus come from the volume change at the dislocation core. Now focusing on the interfacial part farther away from the dislocation core, a smaller negative shift of the $L_3 - e_g$ orbital can be seen as compared to the bottom LAO/STO-s interface. Actually, the interfacial $L_3 - e_g$ shift can be measured from ~ -50 meV at some nanometers from the dislocation to ~ 80 meV in-between the dislocations. Such a spatial distribution seems to correlate with the structural strain distribution but cannot be derived entirely from volume changes since the c/a variations are very small, away from the dislocation core. Furthermore, the energy shift is only observed at the TiO_2 planes close to the interface and might thus be partially associated with orbital ordering, in a similar way as for the LAO/STO-s interface. This suggests that the suppression of the

XLD dichroic signal comes from a blurring of the orbital hierarchy due to the structural heterogeneities at the top interface. We cannot, however, rule out that the different charge confinement at the top interface might affect the orbital order.

DISCUSSION

A recent work has shown that LAO/STO-f interfaces, prepared on homoepitaxial TiO_2 -terminated STO layers, have transport properties similar to those of standard interfaces prepared onto STO substrates.¹³ Such control of the layer fabrication and surface termination allows us to synthesize, here, two n -type LAO/STO interfaces, stacked on top of each other and separated by a p -type STO-f/LAO interface. The microscopic STEM analysis reveals several point defects in the STO film in the vicinity of its two interfaces: the bottom p -type interface displays an excess of Sr, localized in the first unit cells, while the top n -type interface presents a small amount of point defects. While the existence of Sr vacancies cannot be totally excluded, from the investigation of the HAADF contrast and taking into account the literature, oxygen vacancies are more probably the primary point defects present at the top interface. In agreement with the assignment of such point defects, Ti^{3+} at high concentration ($>0.1 \text{ Ti}^{3+}$ per uc) is observed by EELS and XAS and in-gap states are measured by ResPE. It is very likely that electrons are trapped by these defects, changing the whole Ti^{3+} spatial distribution. Similar charge localization due to point defects has been reported for homoepitaxial STO in Sr-rich condition and was shown to be detrimental to the conductivity of the 2DEG.²⁰

At this same top n -type interface, we observe the occurrence of misfit dislocations, which partially relax the LAO layer. The strain relaxation of LAO films on STO substrates is known to depend on the growth conditions, layer thickness,⁵⁵ and the presence of oxygen vacancies in STO;³⁶ in the latter case, the average distance between the dislocations was measured to be approximately 15 nm, comparable with our results. From our microscopic investigation, the presence of vacancies in the STO film next to the second LAO layer is confirmed. Such vacancies, independently if Sr or O vacancies, are known to increase the unit cell volume,^{16,19} and we indeed observed a cell expansion near the top interface up to the last interface plane. Such expansion leads to an increase in the elastic energy required to constrain the top LAO layer, which, therefore, relaxes at thinner layer thickness. A second point, relevant to the formation of misfit dislocations, is the very clear n -type plane termination at this interface, while other interfaces show some degree of intermixing that can contribute to the strain relaxation. These two structural aspects (vacancies and weak interdiffusion) certainly play a role in the occurrence of misfit dislocations at the top interface.

A key difference between the electronic configurations of the two n -type interfaces concerns the absence of the XLD signal for the top interface. Such an XLD signal, usually observed in traditional LAO/STO interfaces, is associated with a strong orbital ordering (d_{xy} orbitals being 100–200 meV below the d_{xz}/d_{yz} ones). The absence of XLD does not arise from the presence of the larger amount of Ti^{3+} (and the presumed oxygen vacancies) near the interface. Indeed, it was shown that a LAO/STO-s interface characterized by a large amount of oxygen vacancies could exhibit an XLD signal larger in amplitude at the interface.⁴⁸

Our STEM-EELS analysis of the top interface indicates heterogeneous crystallographic and electronic structures. The orbital ordering, mainly related to the quantum confinement,^{60,61} can be affected by structural local distortions of the TiO₆ octahedra. An elongation of the TiO₆ octahedron along the *z* axis (increase of *c/a*) lowers the energy of *d_{xz}* and *d_{yz}* orbitals with respect to *d_{xy}* orbitals. *Ab initio* calculations have confirmed that the orbital hierarchy at the LAO/STO interface might be modulated by the application of strain and its resulting octahedral distortion.^{66,67} Nevertheless, such modulation of orbital ordering is small, and our observation of a larger Ti L₃ – *e_g* shift where the *c/a* increases seems contradictory. We suspect that, in our case, the suppression of the orbital hierarchy does not come from the tetragonality change around the Ti atoms. In fact, the strain propagates over several unit cells, while the observed Ti L₃ – *e_g* shift is often constrained to the interface plane. Theoretical calculations have revealed the role of the chemical interface discontinuity on the orbital hierarchy. It appears that the hopping term along the *z* direction accounts for a large fraction of the orbital energy splitting;⁶¹ changing the interface sequence from SrO–TiO₂–La–AlO₂ to SrO–TiO₂–LaO–VO₂ might inverse the orbital order. Similarly, other theoretical work has predicted that a small atomic displacement of the Ti atoms forward or backward the interface is enough to strongly change the hopping term across the interface⁵⁸ and thus to alter the orbital hierarchy. These works provide evidence that the structural inhomogeneity of the last STO-*f* planes can give a strong blurring of the orbital hierarchy as observed by XLD.

CONCLUSION

The comparison between the two *n*-type interfaces in LAO/STO-*f*/LAO/STO-*s* multilayers clearly evidences the interplay between the cation, charge, and structural (point and line defects) reconstructions in the LAO/STO system. The interface between LAO and the STO substrates exhibits characteristics in agreement with the current literature for heterostructures prepared by pulsed laser deposition, i.e., a strained LAO layer, a small amount of Ti³⁺ next to the interface as measured by spectroscopic EELS and XAS and a well-developed orbital hierarchy as inferred by the Ti L_{2,3} XLD measurements. The situation is very different for the interfaces involving STO films where point defects are present. A fraction of the charge is trapped by vacancies, and in-gap states appear near the top interface. The point defects increase the out-of-plane expansion of the lattice parameter, and a network of misfit dislocations relaxes the epitaxial strain on LAO. This structural reconstruction suppresses the hierarchy of *d_{xy}* vs *d_{xz}*/*d_{yz}* orbitals in STO as observed by the XLD measurement. The occurrence of these point defects, in relation with the Sr/Ti or oxygen off-stoichiometry, was already reported for homoepitaxial STO films but seems even more crucial in the case of superlattices where the STO film has to be grown on top of a LAO layer with a *p*-type termination. Furthermore, the strong orbital hierarchy inferred by the energy shift of the Ti L₃ – *e_g* from the STEM-EELS measurement only occurs in a few unit cells very close to the (bottom) interface, suggesting that its origin stems from the highly asymmetric situation of the Ti atoms at the interfacial plane due to the plane sequence AlO₂/LaO/TiO₂/SrO/TiO₂. This suggests the possibility of engineering the orbital hierarchy by controlling the atomic layering.

SUPPLEMENTARY MATERIAL

See the [supplementary material](#) for (I) examples of dislocation for the 800 °C *ex situ* sample, (II) energetic of point defects and clustering in SrTiO₃ and the case of Sr antisite–O vacancy binding energy, (III) B-site displacements measured by HAADF-STEM and typical ABF-STEM imaging at the STO-*s*/LAO/STO-*f* interfaces, (IV) geometrical phase analysis (GPA) for the 800 °C *ex situ* sample, (V) Sr/Ti non stoichiometry for the 800 °C *ex situ* sample, (VI) comparison of Ti³⁺ at the STO-*s*/LAO and STO-*f*/LAO interfaces for the 1100 °C sample, and (VII) multiplet calculation: evolution of the EELS-XAS and XLD signals with the increase in orbital splitting.

ACKNOWLEDGMENTS

The authors acknowledge financial support for STEM microscopy from the European Union Seventh Framework Programme under Grant Agreement No. 312483-ESTEEM2 (Integrated Infrastructure Initiative-I3). This work was supported by the Swiss National Science Foundation (Division II) and the Institut Universitaire de France and received funding from the European Research Council under the European Union Seventh Framework Programme (FP7/2007-2013)/ERC Grant Agreement No. 319286 (Q-MAC). M.C. acknowledges funding from the Swiss National Science Foundation under Grant No. 200021-165529.

REFERENCES

- A. Ohtomo and H. Y. Hwang, *Nature* **427**, 423 (2004).
- N. Reyren, S. Thiel, A. D. Caviglia, L. F. Kourkoutis, G. Hammerl, C. Richter, C. W. Schneider, T. Kopp, A.-S. Rüetschi, D. Jaccard, M. Gabay, D. A. Muller, J.-M. Triscone, and J. Mannhart, *Science* **317**, 1196 (2007).
- A. Caviglia, S. Gariglio, C. Cancellieri, B. Sacépé, A. Fête, N. Reyren, M. Gabay, A. Morpurgo, and J.-M. Triscone, *Phys. Rev. Lett.* **105**, 236802 (2010).
- E. Lesne, Y. Fu, S. Oyarzun, J. C. Rojas-Sánchez, D. C. Vaz, H. Naganuma, G. Sicoli, J.-P. Attané, M. Jamet, E. Jacquet, J.-M. George, A. Barthélémy, H. Jaffrès, A. Fert, M. Bibes, and L. Vila, *Nat. Mater.* **15**, 1261 (2016).
- J.-Y. Chauleau, M. Boselli, S. Gariglio, R. Weil, G. de Loubens, J.-M. Triscone, and M. Viret, *Europhys. Lett.* **116**, 17006 (2016).
- C. Cen, S. Thiel, G. Hammerl, C. W. Schneider, K. E. Andersen, C. S. Hellberg, J. Mannhart, and J. Levy, *Nat. Mater.* **7**, 298 (2008).
- B. Förg, C. Richter, and J. Mannhart, *Appl. Phys. Lett.* **100**, 053506 (2012).
- M. Choi, C. Lin, M. Butcher, C. Rodriguez, Q. He, A. B. Posadas, A. Y. Borisevich, S. Zollner, and A. A. Demkov, *Appl. Phys. Lett.* **106**, 192902 (2015).
- M. Huijben, G. Rijnders, D. H. A. Blank, S. Bals, S. V. Aert, J. Verbeeck, G. Van Tendeloo, A. Brinkman, and H. Hilgenkamp, *Nat. Mater.* **5**, 556 (2006).
- M. Fitzsimmons, N. Hengartner, S. Singh, M. Zhernenkov, F. Bruno, J. Santamaria, A. Brinkman, M. Huijben, H. Molegraaf, J. de la Venta, and I. Schuller, *Phys. Rev. Lett.* **107**, 217201 (2011).
- Z. Salman, O. Ofer, M. Radovic, H. Hao, M. Ben Shalom, K. H. Chow, Y. Dagan, M. D. Hossain, C. D. P. Levy, W. A. MacFarlane, G. M. Morris, L. Patthey, M. R. Pearson, H. Saadaoui, T. Schmitt, D. Wang, and R. F. Kiefl, *Phys. Rev. Lett.* **109**, 257207 (2012).
- J. E. Ortmann, S. Kwon, A. B. Posadas, M. J. Kim, and A. A. Demkov, *J. Appl. Phys.* **125**, 155302 (2019).
- D. Li, S. Gariglio, C. Cancellieri, A. Fête, D. Stornaiuolo, and J.-M. Triscone, *APL Mater.* **2**, 012102 (2014).
- H. Lee, N. Campbell, J. Lee, T. J. Asel, T. R. Paudel, H. Zhou, J. W. Lee, B. Noesges, J. Seo, B. Park, L. J. Brillson, S. H. Oh, E. Y. Tsybal, M. S. Rzchowski, and C. B. Eom, *Nat. Mater.* **17**, 231 (2018).
- T. Suzuki, Y. Nishi, and M. Fujimoto, *Philos. Mag. A* **80**, 621 (2000).

- ¹⁶C. M. Brooks, L. F. Kourkoutis, T. Heeg, J. Schubert, D. A. Muller, and D. G. Schlom, *Appl. Phys. Lett.* **94**, 162905 (2009).
- ¹⁷D. J. Keeble, S. Wicklein, R. Dittmann, L. Ravelli, R. A. Mackie, and W. Egger, *Phys. Rev. Lett.* **105**, 226102 (2010).
- ¹⁸Y. Tokuda, S. Kobayashi, T. Ohnishi, T. Mizoguchi, N. Shibata, Y. Ikuhara, and T. Yamamoto, *Appl. Phys. Lett.* **99**, 033110 (2011).
- ¹⁹D. J. Keeble, S. Wicklein, L. Jin, C. L. Jia, W. Egger, and R. Dittmann, *Phys. Rev. B* **87**, 195409 (2013).
- ²⁰M. L. Reinle-Schmitt, C. Cancellieri, A. Cavallaro, G. F. Harrington, S. J. Leake, E. Pomjakushina, J. A. Kilner, and P. R. Willmott, *Nanoscale* **6**, 2598 (2014).
- ²¹N. Nakagawa, H. Y. Hwang, and D. A. Muller, *Nat. Mater.* **5**, 204 (2006).
- ²²A. K. Singh, T. C. Wu, M. C. Chen, M. Y. Song, W. L. Lee, C. P. Su, and M. W. Chu, *Phys. Rev. Mater.* **2**, 114009 (2018).
- ²³C. Cancellieri, D. Fontaine, S. Gariglio, N. Reyren, A. Caviglia, A. Fête, S. Leake, S. Pauli, P. Willmott, M. Stengel, P. Ghosez, and J.-M. Triscone, *Phys. Rev. Lett.* **107**, 056102 (2011).
- ²⁴C. Bell, S. Harashima, Y. Hikita, and H. Y. Hwang, *Appl. Phys. Lett.* **94**, 222111 (2009).
- ²⁵E. Stavitski and F. M. F. de Groot, *Micron* **41**, 687 (2010).
- ²⁶V. N. Strocov, X. Wang, M. Shi, M. Kobayashi, J. Krempasky, C. Hess, T. Schmitt, and L. Patthey, *J. Synchr. Rad.* **21**, 32 (2014).
- ²⁷S. Clark, M. Segall, C. Pickard, P. Hasnip, M. Probert, K. Refson, and M. Payne, *Z. Kristallogr. - Cryst. Mater.* **220**, 567 (2005), reproduced with permission from the publisher.
- ²⁸D. M. Ceperley and B. J. Alder, *Phys. Rev. Lett.* **45**, 566 (1980).
- ²⁹T. Ohnishi, K. Shibuya, T. Yamamoto, and M. Lippmaa, *J. Appl. Phys.* **103**, 103703 (2008).
- ³⁰M. Choi, F. Oba, and I. Tanaka, *Phys. Rev. Lett.* **103**, 185502 (2009).
- ³¹D. Lee, H. Lu, Y. Gu, S. Y. Choi, S. D. Li, S. Ryu, T. R. Paudel, K. Song, E. Mikheev, S. Lee, S. Stemmer, D. A. Tenne, S. H. Oh, E. Y. Tsymlal, X. Wu, L. Q. Chen, A. Gruverman, and C. B. Eom, *Science* **349**, 1314 (2015).
- ³²K. Klyukin and V. Alexandrov, *Phys. Rev. B* **95**, 035301 (2017).
- ³³L. Yu and A. Zunger, *Nat. Commun.* **5**, 5118 (2014).
- ³⁴B. Liu, V. R. Cooper, H. Xu, H. Xiao, Y. Zhang, and W. J. Weber, *Phys. Chem. Chem. Phys.* **16**, 15590 (2014).
- ³⁵C. Xu, C. Bäumer, R. A. Heinen, S. Hoffmann-Eifert, F. Gunkel, and R. Dittmann, *Sci. Rep.* **6**, 22410 (2016).
- ³⁶A. Kalabukhov, R. Gunnarsson, J. Borjesson, E. Olsson, T. Claeson, and D. Winkle, *Phys. Rev. B* **75**, 121404 (2007).
- ³⁷M. J. Hÿtch, E. Snoeck, and R. Kilaas, *Ultramicroscopy* **74**, 131 (1998).
- ³⁸J.-L. Maurice, C. Carrétéro, M.-J. Casanove, K. Bouzouane, S. Guyard, É. Larquet, and J.-P. Contour, *Phys. Status Solidi A* **203**, 2209 (2006).
- ³⁹C. L. Jia, S. B. Mi, M. Faley, U. Poppe, J. Schubert, and K. Urban, *Phys. Rev. B* **79**, 081405 (2009).
- ⁴⁰C. Cantoni, J. Gazquez, F. Miletto Granozio, M. P. Oxley, M. Varela, A. R. Lupini, S. J. Pennycook, C. Aruta, U. S. di Uccio, P. Perna, and D. Maccariello, *Adv. Mater.* **24**, 3952 (2012).
- ⁴¹J. Lee, J. K. Choi, S. Y. Moon, J. Park, J.-S. Kim, C. S. Hwang, S.-H. Baek, J.-H. Choi, and H. J. Chang, *Appl. Phys. Lett.* **106**, 071601 (2015).
- ⁴²P. W. Lee, V. N. Singh, G. Y. Guo, H.-J. Liu, J.-C. Lin, Y.-H. Chu, C. H. Chen, and M.-W. Chu, *Nat. Commun.* **7**, 12773 (2016).
- ⁴³J. Gazquez, M. Stengel, R. Mishra, M. Scigaj, M. Varela, M. A. Roldan, J. Fontcuberta, F. Sánchez, and G. Herranz, *Phys. Rev. Lett.* **119**, 106102 (2017).
- ⁴⁴M. Takizawa, S. Tsuda, T. Susaki, H. Y. Hwang, and A. Fujimori, *Phys. Rev. B* **84**, 245124 (2011).
- ⁴⁵Y. Y. Chu, Y. F. Liao, V. T. Tra, J. C. Yang, W. Z. Liu, Y. H. Chu, J. Y. Lin, J. H. Huang, J. Weinen, S. Agrestini, K.-D. Tsuei, and D. J. Huang, *Appl. Phys. Lett.* **99**, 262101 (2011).
- ⁴⁶G. Berner, S. Glawion, J. Walde, F. Pfaff, H. Hollmark, L. C. Duda, S. Paetel, C. Richter, J. Mannhart, M. Sing, and R. Claessen, *Phys. Rev. B* **82**, 241405 (2010).
- ⁴⁷M. Salluzzo, J. C. Cezar, N. B. Brookes, V. Bisogni, G. M. De Luca, C. Richter, S. Thiel, J. Mannhart, M. Huijben, A. Brinkman, G. Rijnders, and G. Ghiringhelli, *Phys. Rev. Lett.* **102**, 166804 (2009).
- ⁴⁸M. Salluzzo, S. Gariglio, D. Stornaiuolo, V. Sessi, S. Rusponi, C. Piamonteze, G. M. De Luca, M. Minola, D. Marré, A. Gadaleta, H. Brune, F. Nolting, N. B. Brookes, and G. Ghiringhelli, *Phys. Rev. Lett.* **111**, 087204 (2013).
- ⁴⁹D. Pesquera, M. Scigaj, P. Gargiani, A. Barla, J. Herrero-Martín, E. Pellegrin, S. M. Valvidares, J. Gázquez, M. Varela, N. Dix, J. Fontcuberta, F. Sánchez, and G. Herranz, *Phys. Rev. Lett.* **113**, 156802 (2014).
- ⁵⁰A. Fujimori, A. E. Bocquet, K. Morikawa, K. Kobayashi, T. Saitoh, Y. Tokura, I. Hase, and M. Onoda, *J. Phys. Chem. Solids* **57**, 1379 (1996).
- ⁵¹Y. Ishida, R. Eguchi, M. Matsunami, K. Horiba, M. Taguchi, A. Chainani, Y. Senba, H. Ohashi, H. Ohta, and S. Shin, *Phys. Rev. Lett.* **100**, 056401 (2008).
- ⁵²A. Chikina, F. Lechermann, M.-A. Husanu, M. Caputo, C. Cancellieri, X. Wang, T. Schmitt, M. Radovic, and V. N. Strocov, *ACS Nano* **12**, 7927 (2018).
- ⁵³N. Pavlenko, T. Kopp, E. Y. Tsymlal, J. Mannhart, and G. A. Sawatzky, *Phys. Rev. B* **86**, 064431 (2012).
- ⁵⁴G. Berner, M. Sing, H. Fujiwara, A. Yasui, Y. Saitoh, A. Yamasaki, Y. Nishitani, A. Sekiyama, N. Pavlenko, T. Kopp, C. Richter, J. Mannhart, S. Suga, and R. Claessen, *Phys. Rev. Lett.* **110**, 247601 (2013).
- ⁵⁵P. Schütz, D. V. Christensen, V. Borisov, F. Pfaff, P. Scheiderer, L. Dudy, M. Zapf, J. Gabel, Y. Z. Chen, N. Pryds, V. A. Rogalev, V. N. Strocov, C. Schlueter, T.-L. Lee, H. O. Jeschke, R. Valentí, M. Sing, and R. Claessen, *Phys. Rev. B* **96**, 161409(R) (2017).
- ⁵⁶C. Cancellieri, M. L. Reinle-Schmitt, M. Kobayashi, V. N. Strocov, P. R. Willmott, D. Fontaine, P. Ghosez, A. Filippetti, P. Delugas, and V. Fiorentini, *Phys. Rev. B* **89**, 121412 (2014).
- ⁵⁷V. N. Strocov, C. Cancellieri, and A. S. Mishchenko, in *Spectroscopy of Complex Oxide Interfaces: Photoemission and Related Spectroscopies*, edited by C. Cancellieri and V. N. Strocov (Springer-Verlag, 2018).
- ⁵⁸H. Chen, A. M. Kolpak, and S. Ismail-Beigi, *Phys. Rev. B* **79**, 161402 (2009).
- ⁵⁹M. Stengel, *Phys. Rev. Lett.* **106**, 136803 (2011).
- ⁶⁰P. Delugas, A. Filippetti, V. Fiorentini, D. I. Bilc, D. Fontaine, and P. Ghosez, *Phys. Rev. Lett.* **106**, 166807 (2011).
- ⁶¹Z. Zhong, P. Wissgott, K. Held, and G. Sangiovanni, *Europhys. Lett.* **99**, 37011 (2012).
- ⁶²Z. Zhong, A. Tóth, and K. Held, *Phys. Rev. B* **87**, 161102 (2013).
- ⁶³Z. Popović, S. Satpathy, and R. Martin, *Phys. Rev. Lett.* **101**, 256801 (2008).
- ⁶⁴L. Shulenburg, S. Y. Savrasov, and R. E. Cohen, *J. Phys.: Conf. Ser.* **215**, 012122 (2010).
- ⁶⁵G. Liu, Q. Lei, M. A. Wolak, Q. Li, L.-Q. Chen, C. Winkler, J. Sloppy, M. L. Taheri, and X. Xi, *J. Appl. Phys.* **120**, 085302 (2016).
- ⁶⁶S. Nazir, M. Behtash, and K. Yang, *RSC Adv.* **5**, 15682 (2015).
- ⁶⁷M. Behtash, S. Nazir, Y. Wang, and K. Yang, *Phys. Chem. Chem. Phys.* **18**, 6831 (2016).